# Microwave spectra of the leading and trailing hemispheres of Iapetus

Léa Bonnefoy, Emmanuel Lellouch, Alice Le Gall, Jean-François Lestrade, Raphaël Moreno, Bryan Butler, Jérémie Boissier, Cédric Leyrat, Robin Sultana, Thibault Cavalié, et al.

# Journal Pre-proof

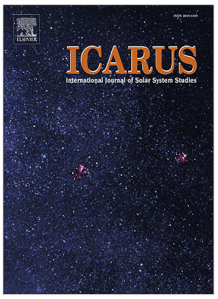


Microwave spectra of the leading and trailing hemispheres of Iapetus

Léa E. Bonnefoy, Emmanuel Lellouch, Alice Le Gall,
Jean-François Lestrade, Raphaël Moreno, Bryan Butler,
Jérémie Boissier, Cédric Leyrat, Robin Sultana, Thibault Cavalié,
Mark Gurwell, Arielle Moullet, Bilal Ladjelate, Nicolas Ponthieu

PII: S0019-1035(24)00008-3
DOI: https://doi.org/10.1016/j.icarus.2024.115950
Reference: YICAR 115950

To appear in: *Icarus*

Received date : 30 August 2023
Revised date : 22 December 2023
Accepted date : 5 January 2024

Please cite this article as: L.E. Bonnefoy, E. Lellouch, A. Le Gall et al., Microwave spectra of the leading and trailing hemispheres of Iapetus. *Icarus* (2024), doi: https://doi.org/10.1016/j.icarus.2024.115950.

Draft version December 22, 2023
Typeset using LaTeX **manuscript** style in AASTeX631

# Microwave Spectra of the Leading and Trailing Hemispheres of Iapetus

Léa E. Bonnefoy,[1,2,3] Emmanuel Lellouch,[3] Alice Le Gall,[2,4] Jean-François Lestrade,[1] Raphaël Moreno,[3] Bryan Butler,[5] Jérémie Boissier,[6] Cédric Leyrat,[3] Robin Sultana,[2] Thibault Cavalié,[7,3] Mark Gurwell,[8] Arielle Moullet,[9] Bilal Ladjelate,[10] and Nicolas Ponthieu[11]

[1]*LERMA, Observatoire de Paris, PSL Research University, CNRS, Sorbonne Universités, Univ. Paris Cité, F-75014 Paris, France*

[2]*Laboratoire Atmosphères, Milieux, Observations Spatiales (LATMOS), UVSQ/CNRS/Paris VI, UMR 8190, 78280 Guyancourt, France*

[3]*LESIA, Observatoire de Paris, PSL Research University, CNRS, Sorbonne Université, Univ. Paris 06, Univ. Paris Cité, Sorbonne Paris Cité, 92195 Meudon, France*

[4]*Institut Universitaire de France, Paris, France*

[5]*National Radio Astronomy Observatory, Socorro, NM, USA*

[6]*Institut de Radioastronomie Millimetrique, 300 rue de la Piscine, F-38406 Saint Martin d'Heres, France*

[7]*University of Bordeaux, CNRS, LAB, UMR 5804, Pessac, France*

[8]*Center for Astrophysics | Harvard & Smithsonian, Cambridge, MA, USA*

[9]*SOFIA Science Center, Moffett Field, CA, USA*

[10]*Instituto de Radio Astronomía Milimétrica, Avenida Divina Pastora, 7 Núcleo Central, 18012 Granada, Spain*

[11]*Univ. Grenoble Alpes, CNRS, IPAG, 38000 Grenoble, France*

## ABSTRACT

The leading hemisphere of Saturn's synchronous moon Iapetus is covered by a low-albedo material, contrasting with its bright trailing hemisphere. This dichotomy is also apparent in radar and microwave radiometry observations, which are sensitive to the properties of the near subsurface. To better understand the regional properties of Iapetus and their variations with depth, we assemble the microwave spectra of its leading and trailing hemispheres. Pre-existing data are combined with new millimetric and centimetric observations acquired with the IRAM 30-meter dish, IRAM NOEMA interferometer, and VLA interferometer. These data, interpreted with the help of a model with vertically uniform thermal properties, reveal

complex variations in structure and/or composition with depth on the leading side. Meanwhile, the trailing side emissivity is found to be especially low at all observed frequencies, indicating efficient scattering processes on subsurface structures, as observed on Saturn's other icy moons. We also report the first observations of Saturn's retrograde moon Phoebe at these frequencies, which has an emissivity higher than that of the trailing hemisphere of Iapetus and similar to its dark leading side, consistent with the theory that Phoebe is the source of the dark material on Iapetus.

## 1. INTRODUCTION

The most salient attribute of Iapetus is its leading/trailing hemispheric albedo dichotomy, the most dramatic one in the Solar System, first noticed at the time of its discovery in 1671 by G. D. Cassini. Saturn's moon Iapetus is in synchronous rotation and orbits at 61 $R_{Saturn}$ (Table 1), within the Phoebe ring, whose retrograde particles spiral toward Saturn. Thus Iapetus's leading hemisphere (LH) accumulates a coating of dark material, while its trailing side remains mostly icy and bright (Burns et al. 1996; Tamayo et al. 2011). However, the dark material on Iapetus extends slightly beyond the leading hemisphere at equatorial latitudes, and is absent from the poles. This distribution is consistent with thermal segregation: albedo differences cause significant temperature contrasts, which lead to migration of water ice from dark, warmer regions to bright, colder ones, in particular toward the poles (Hendrix & Hansen 2008; Spencer & Denk 2010; Kimura et al. 2011).

The trailing hemisphere (TH) of Iapetus has a mainly icy composition including the presence of some $CO_2$, while the dark terrain on the leading hemisphere (LH) presents spectral features of metallic iron and iron-bearing minerals (hematite), $CO_2$, and water ice, similar to Phoebe's surface (Fink et al. 1976; Buratti et al. 2005; Pinilla-Alonso et al. 2011; Clark et al. 2012). More recent studies show the presence of aromatic and aliphatic hydrocarbons on Phoebe, Iapetus's leading hemisphere, and Hyperion, also consistent with a dust coating from Phoebe (Cruikshank et al. 2014; Hendrix et al. 2018). The Cassini Composite InfraRed Spectrometer (CIRS), which observed Iapetus in the thermal infrared (0.16 to 1 mm wavelength), revealed

**Table 1.** Orbital characteristics and bolometric Bond albedos of Iapetus and Phoebe, from Castillo-Rogez et al. (2018); Thomas et al. (2018); Blackburn et al. (2011); Howett et al. (2010). Iapetus, unlike Phoebe, is synchronous: it has identical orbital and rotation periods.

| Satellite | Mean Radius (km) | Semi-major axis ($R_{Saturn}$ [a]) | Orbital period (days) | Rotation period $P_{day}$ (days) | Bond albedo | Mean density (kg m$^{-3}$) |
|---|---|---|---|---|---|---|
| Iapetus | 734.3 ± 2.8 | 61.1 | 79.33 | 79.33 | 0.01 to 0.41 | 1088 ± 13 |
| Phoebe | 106.5 ± 0.7 | 221.0 | 548.02 | 0.39 | 0.1 | 1642 ± 18 |

[a] $R_{Saturn}$ is Saturn's equatorial radius, namely 60330 km.

differences in albedo and thermal inertia between the leading and trailing sides and points to a dark material thickness of 7 to 16 cm (Howett et al. 2010; Rivera-Valentin et al. 2011). The hemispheric dichotomy is also obvious in Cassini radar and radiometry data, at 2.2 cm wavelength, whereas it is invisible to 13.6 cm Arecibo radar observations, suggesting a leading side dark material thickness of the order of tens of centimeters, but not exceeding a meter (Black et al. 2004; Ostro et al. 2006; Le Gall et al. 2014). Yet the thickness of the dark material layer and the vertical structure (porosity, grain size, composition) of the subsurface on both hemispheres remains uncertain.

Because longer wavelengths probe deeper into the subsurface, observing a surface at a variety of wavelengths can bring to light changes in thermal, compositional, and physical properties with depth. At its orbital radius, the maximum elongation of Iapetus from Saturn is about 8 to 9 arc minutes as seen from Earth: its flux density can thus be separated from the planet's with several ground-based radiotelescopes. Using the NIKA2 (New IRAM KIDs Array) dual band camera on the IRAM (Institut de Radioastronomie Millimétrique) 30-meter telescope, the NOEMA (Northern Extended Millimeter Array) interferometer, and the VLA (Very Large Array), new observations of the leading and trailing sides of Iapetus have been acquired and calibrated. In combination with pre-existing datasets from Cassini and other ground-based telescopes, the newly derived disk-integrated brightness temperature ($T_B^{\rm disk}$) spectra reveal distinct leading and trailing hemisphere physical properties, with unexpected behaviors at millimeter wavelengths.

## 2. PRE-EXISTING IAPETUS MICROWAVE RADIOMETRY OBSERVATIONS

Prior to the present study, the brightness temperature of Iapetus had been measured at millimeter-to-centimeter wavelengths using three different instruments: the Submillimeter Array, the Green Bank Telescope, and the Cassini radiometer. These observations and associated results are summarized in this section.

### 2.1. *Submillimeter Array (SMA) observations*

A series of 13 observations of Iapetus were conducted with the SMA in Hawaii in 2012, in order to characterize the emissivity of the leading and trailing hemisphere terrains at a wavelength of 1.3 mm (225 GHz frequency). Four of these observations were calibrated and presented by Hagen et al. (2014), showing a warmer LH than TH. From a comparison with a thermal model and using Cassini CIRS observations to constrain the surface temperature, Hagen et al. (2014) found that a LH emissivity of $e_{\rm LH}^{1.3\ \rm mm} = 0.759$ and a TH emissivity of $e_{\rm TH}^{1.3\ \rm mm} = 0.602$ would be consistent with Cassini CIRS data.

The remaining SMA observations of Iapetus have since been calibrated (M. Gurwell and A. Moullet, 2020, personal communication); Titan was used as a primary calibrator. From these flux densities, we derive $T_B^{\rm disk}$ using the method detailed in Section 3.1. These data are presented in Table 2, shown in Fig. 1. The leading/trailing dichotomy is clearly visible in the resulting lightcurve, yielding average LH ($-90 \pm 50$°E) and TH ($+90 \pm 50$°E) disk-integrated brightness temperatures of $< T_B^{\rm disk} >_{\rm LH} = 84.2 \pm 1.9$ K and $< T_B^{\rm disk} >_{\rm TH} = 63.9 \pm 2.1$ K, respectively. The remaining longitudes ($0 \pm 40$°E and $180 \pm 40$° E) contain a mixture of LH and TH material, and are considered "mixed". The LH and TH $T_B^{disk}$ values are consistent with those found by Hagen et al. (2014) from a subset of the same dataset. The SMA observations are further discussed in Section 4.2.

### 2.2. *Green Bank Telescope (GBT) observations*

Ries (2012) partially bridged the gap between microwave and Cassini thermal infrared radiometry by observing Iapetus's LH and TH at wavelengths varying from 3.3 to 10.8 mm using the Green Bank

Telescope (GBT), a 100-meter single dish radiotelescope located in Green Bank, West Virginia (USA). At 3.3 mm (90 GHz; W band), the MUSTANG (MUltiplexed Squid Transition-edge sensor Array at Ninety Gigahertz) imaging bolometer array acquired observations on the LH and at 30°E (mixed dark and bright terrains, but dominantly TH). At 7.8, 8.6, 9.6, and 10.8 mm (38.25, 34.75, 31.25, and 27.75 GHz), the CCB (Caltech Continuum Backend) Ka-band receiver observed a variety of regions of Iapetus on 11 different occasions, four of which failed due to bad weather. Three observations had the best weather and are considered reliable by Ries (2012); two of these are on the LH and one on the TH. The main characteristics of the most reliable data gathered with the GBT are presented in Table 2 and shown in Fig. 1; for further detail, including on the calibration, atmosphere removal, and sidelobe mitigation techniques, see Ries (2012). Ries (2012) then used an empirical thermal model with sub-solar heating (but no seasonal effects) to derive the emissivity. This unique and valuable dataset nonetheless has large uncertainties and presents some inconsistency between leading hemisphere observations acquired on different days at 9.6 and 7.8 mm. Similarly, the trailing hemisphere data shows an unexpected (and suspicious, given the large uncertainties) jump of > 13 K from 8.6 to 9.6 mm.

On the leading side, Ries (2012) observed decreasing $T_B$ and emissivities with increasing wavelength. They attributed this effect to a thermal depth effect, i.e. to longer wavelengths probing deeper into the dayside's cold subsurface, below the diurnal skin depth. On the trailing side, Ries (2012) observed a potential wide absorption feature, with anomalously low temperatures possibly centered at 3 mm. By comparison with outputs from the semi-empirical Microwave Emission Model for Layered Snowpacks (MEMLS) developed for and tested on snow on Earth (Wiesmann et al. 1998), Ries (2012) attributed this feature to losses due to diffuse scattering by 1–2-mm ice particles.

### 2.3. *Cassini radiometer observations*

The Cassini-Huygens mission, which was in orbit around Saturn from 2004 to 2017, included a 2.2-cm wavelength (13.8 GHz, Ku-band; Elachi et al. 2004) radar/radiometer which acquired Iapetus observations during four flybys. These data have been analyzed in detail by Le Gall et al. (2014), who found that the LH/TH dichotomy is obvious in the 2.2-cm radiometry, which likely also probes the icy substrate present

below the dark material of the trailing side. To examine the leading and trailing spectra of Iapetus, we use only the data acquired during IA049 (the Cassini Iapetus flyby during the 49th Saturn orbit), which includes disk-integrated observations centered on the leading and trailing hemispheres. These data, which have recently been re-calibrated by Le Gall et al. (2023), are provided in Table 2 and included in Fig. 1. All Earth-based observations were acquired near local noon at the apparent disk center, whereas the two Cassini radiometry scans represented here have a local time at the sub-spacecraft point of 21:49 (IA049-2, on the leading side) and 09:54 (IA049-4, on the trailing side). This means that the Cassini brightness temperatures are not directly comparable with the Earth-based data, but having both night and day observations adds a useful constraint when using a thermal model to fit the datasets simultaneously and examine their emissivities.

**Table 2**. Observations of Iapetus pre-dating the observation campaign presented herein, from Ries (2012), Le Gall et al. (2014), Hagen et al. (2014), and Gurwell and Moullet (2020, personal communication). All sub-Earth coordinates and disk-integrated brightness temperatures $T_B^{\rm disk}$ were re-calculated from the information provided by these references. The target's heliocentric distance $r_h$, which affects the $T_B$ by up to 5%, is also given.

| Date | $r_h$ (AU) | $\lambda$ (mm) | Lat. (°N) | Long. (°E) | Region | Flux density (mJy) | $T_B^{\rm disk}$ (K) |
|---|---|---|---|---|---|---|---|
| Submillimeter Array observations (Gurwell and Moullet, 2020, personal communication) | | | | | | | |
| 23 Feb 2011[a] | 9.58 | 1.33 | 13 | -140 | LH | 124.0 ± 11.3 | 88.3 ± 7.6 |
| 28 Feb 2012 | 9.73 | 1.33 | 15 | -6 | Mixed | 97.1 ± 3.2 | 74.2 ± 2.3 |
| 11 May 2012 | 9.75 | 1.27 | 14 | 20 | Mixed | 112.4 ± 3.5 | 74.6 ± 2.2 |
| 24 May 2012 | 9.75 | 1.33 | 14 | -40 | LH | 113.1 ± 4.2 | 83.3 ± 2.9 |
| 26 May 2012 | 9.75 | 1.33 | 14 | -48 | LH | 115.5 ± 5.9 | 85.1 ± 4.1 |
| 26 May 2012 | 9.75 | 1.33 | 14 | -49 | LH | 115.8 ± 3.9 | 85.4 ± 2.7 |
| 02 Jun 2012 | 9.74 | 1.33 | 14 | -80 | LH | 112.2 ± 3.7 | 84.5 ± 2.6 |
| 16 Jun 2012 | 9.72 | 1.33 | 14 | -144 | LH | 99.7 ± 7.2 | 78.4 ± 5.2 |
| 09 Jul 2012[b] | 9.74 | 1.33 | 14 | 111 | TH | 76.9 ± 4.0 | 66.0 ± 3.1 |
| 12 Jul 2012 | 9.74 | 1.33 | 14 | 97 | TH | 69.9 ± 3.0 | 61.1 ± 2.4 |
| 13 Jul 2012 | 9.74 | 1.33 | 14 | 93 | TH | 74.8 ± 2.5 | 65.3 ± 2.0 |
| 26 Jul 2012[b] | 9.77 | 1.33 | 14 | 34 | Mixed | 71.7 ± 4.6 | 65.6 ± 3.9 |

**Table 2** *continued on next page*

**Table 2** *(continued)*

| Date | $r_h$ (AU) | $\lambda$ (mm) | Lat. (°N) | Long. (°E) | Region | Flux density (mJy) | $T_B^{\rm disk}$ (K) |
|---|---|---|---|---|---|---|---|
| 21 Aug 2012[a] | 9.76 | 1.33 | 14 | -81 | LH | 89.9 ± 12.3 | 86.9 ± 11.1 |
| Green Bank Telescope observations (Ries 2012) | | | | | | | |
| 03 Mar 2010 | 9.51 | 3.33 | 10 | 30 | Mixed | 16.5 ± 2.5 | 66.2 ± 9.7 |
| 16 Feb 2011 | 9.60 | 3.33 | 13 | -104 | LH | 23.1 ± 1.0 | 100.4 ± 4.2 |
| 04 Dec 2010 | 9.56 | 10.8 | 13 | -131 | LH | 1.04 ± 0.22 | 62.3 ± 12.6 |
| | | 9.6 | | | | 1.64 ± 0.16 | 76.8 ± 7.2 |
| | | 8.6 | | | | 1.79 ± 0.13 | 68.1 ± 4.7 |
| | | 7.8 | | | | 2.78 ± 0.25 | 86.6 ± 7.5 |
| 06 May 2011 | 9.62 | 10.8 | 12 | -108 | LH | 1.77 ± 0.05 | 79.7 ± 2.2 |
| | | 9.6 | | | | 2.34 ± 0.05 | 83.0 ± 1.7 |
| | | 8.6 | | | | 2.84 ± 0.05 | 81.5 ± 1.4 |
| | | 7.8 | | | | 3.57 ± 0.08 | 84.5 ± 1.8 |
| 19 Nov 2011 | 9.68 | 10.8 | 14 | 91 | TH | 0.94 ± 0.28 | 61.38 ± 17.6 |
| | | 9.6 | | | | 1.13 ± 0.13 | 58.3 ± 6.4 |
| | | 8.6 | | | | 1.06 ± 0.11 | 44.9 ± 4.4 |
| | | 7.8 | | | | 1.25 ± 0.13 | 43.8 ± 4.3 |
| Cassini radiometer observations (Le Gall et al. 2014) | | | | | | | |
| 10 Sep 2007 | 9.22 | 22 | 12 | -69 | LH | | 77.4 ± 0.9 |
| 11 Sep 2007 | 9.22 | 22 | -12 | 107 | TH | | 62.6 ± 0.8 |

[a] Due to poor weather, these observations are less reliable.

[b] Due to the proximity of Titan to Saturn, calibration was difficult and a 5% absolute error was added.

### 2.4. *Outstanding questions and motivations for the present study*

The microwave radiometry data gathered from Cassini, the GBT, and the SMA reveals compositional and structural variations with wavelength and thus depth, on both sides of Iapetus. However, these observations also pose new questions.

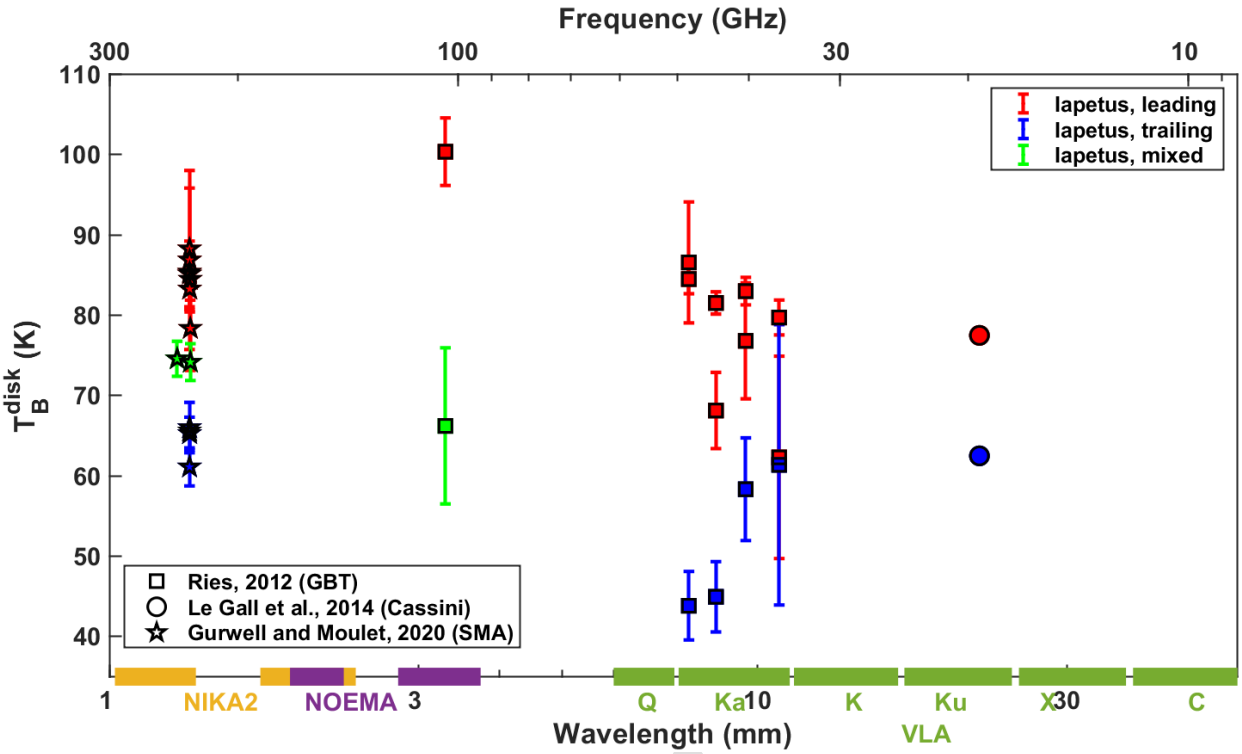


**Figure 1.** Compilation of Iapetus disk-integrated brightness temperatures $T_B^{disk}$ from pre-2017 observations, using the SMA (Hagen et al. 2014, and recalibrated by Gurwell and Moullet, 2020, personal communication), the GBT (Ries 2012), and the Cassini radiometer (Le Gall et al. 2014). Note that although the distance to the Sun varies by up to 12% from perihelion to aphelion, it only changes $T_B^{disk}$ by $< 5$ K. The uncertainties for the Cassini data are smaller than the points (see Table 2). The frequency bands of the Iapetus daata acquired with the NIKA2, NOEMA, and VLA observatories are indicated.

On the leading side, the 1.3 mm $T_B^{\rm disk}$ are 15 K lower than measured by the GBT at 3.3 mm, but are within uncertainties of the 7.8 mm measurements. While a thermal depth effect may still be decreasing $T_B^{\rm disk}$ at the longer wavelengths, another process must be causing the 3.3-mm peak. Such a steep positive slope is difficult to explain, and casts doubt on the very high 3.3-mm value, which relies on a single measurement with a telescope designed for longer wavelengths. Meanwhile, on the trailing side, more data is required to verify and characterize the possible absorption by scattering feature, centered near 3 mm, identified by Ries (2012).

At centimeter wavelengths, the leading and trailing spectra become more and more similar with increasing wavelength. This observation is consistent with the active radar data, where the hemispheres are different at 2.2 cm but identical at 13.6 cm (Black et al. 2004; Ostro et al. 2006). It is therefore likely that, at a certain wavelength long enough to probe dominantly the icy substrate, the thin surface dark material layer will become insignificant in comparison, and both sides will have the same brightness temperature. The transition in radiometry data is likely to be progressive due to the possibility of a mixed ice/dust layer, the fact that radiometry integrates over many depths rather than senses a specific depth, and the fact that vertical observations (at the center of the disk) probe deeper than oblique observations (near the edge).

If confirmed, what is the cause behind the increasing 1.3 – 3.3 mm wavelength values of $T_B^{\rm disk}$ on the leading side? Can further observations help quantify the particle size causing the trailing hemisphere mm-wavelength dip in $T_B^{\rm disk}$? At what wavelength, if any, do the leading and trailing hemispheres have the same temperature and emissivity? Does microwave radiometry support the hypothesis that the Phoebe ring is the source of the leading hemisphere dark material?

## 3. OBSERVATION CAMPAIGN AND NEW OBSERVATIONS

To help address these questions and complete Iapetus's microwave spectrum, we conducted an observation campaign in the mm and cm domains. We observed the two faces of Iapetus at 1.15 and 2.0 mm using the NIKA2 dual band camera on the IRAM-30 m telescope at Pico Veleta in Spain (Section 3.2). The IRAM NOEMA interferometer located in the Plateau de Bure in France allowed us to observe both hemispheres of Iapetus at 2 and 3 mm (Section 3.3). In parallel, centimetric data were acquired on Iapetus and Phoebe using the VLA interferometer in New Mexico, USA (Section 3.4).

### 3.1. *Deriving disk-integrated brightness temperature*

Radiotelescopes generally measure, at a frequency $\nu$, a flux density $S_\nu$ (in units of Jansky, where 1Jy = $10^{-26}$W m$^{-2}$ Hz$^{-1}$), equal to the product of the spectral radiance $B_\nu^{\rm target}$ of the target and its solid angle $\Omega^{\rm target}$ as seen from the observer (for an unresolved source). The flux density of a target is measured in contrast to the cosmic microwave background (CMB) radiation $B_\nu^{\rm CMB}$. The CMB's signal must then be sub-

tracted as follows, especially at longer (centimeter) wavelengths where it contributes a possibly significant fraction of the measured flux density:

$$S_\nu = (B_\nu^{\text{target}} - B_\nu^{\text{CMB}}) \times \Omega^{\text{target}} \quad (1)$$

By inserting the formula for solid angle and Planck's equation for spectral radiance, we find:

$$S_\nu = \frac{2h\nu^3}{c^2}\left(\frac{1}{e^{h\nu/k_B T_B^{\text{disk}}} - 1} - \frac{1}{e^{h\nu/k_B T_{\text{CMB}}} - 1}\right) \times \frac{\pi R_{eq} R'_p}{D^2} \quad (2)$$

where $T_{\text{CMB}} = 2.725$ K is the temperature of the CMB, $D$ is the distance from the telescope to the target, $R_{eq}$ is the equatorial radius (see Table 1), and $\nu$ is the effective frequency, found by convolving the receiving bandwidth with the atmospheric transmission. $R'_p$ is the projected polar radius of Iapetus, which depends on the sub-Earth latitude $\phi$ and the polar radius $R_p$ (712.4 km in the case of Iapetus) as follows:

$$R'_p = \sqrt{R_{eq}^2 \sin^2\phi + R_p^2 \cos^2\phi} \quad (3)$$

The disk-integrated brightness temperature $T_B^{\text{disk}}$ can then be derived by inverting Eq. 2.

### 3.2. *IRAM 30 meter telescope NIKA2 observations*

Observations were conducted with the NIKA2 dual band millimetre camera installed on the IRAM 30-meter telescope at Pico Veleta (altitude 2850m) in Spain (Monfardini et al. 2014; Catalano et al. 2014; Calvo et al. 2016; Adam et al. 2018; Perotto et al. 2020). NIKA2 is operating with kinetic inductance detectors arranged into three arrays: two with a maximum transmission around 260 GHz (1.15 mm) with 1140 detectors in each polarization, and one at 150 GHz (2.0 mm) with 616 detectors at a single polarization. The transmission bands of the detectors are broad with a 50 GHz full width at half maximum transmission at both wavelengths. The combination of its large field of view (6.5 x 6.5 arcminutes) and high sensitivity provides the NIKA2 camera with a high mapping speed. The angular resolutions (main beam FWHM) are 17.7 and 11.2 arcseconds at 150 and 260 GHz, respectively.

**Table 3.** Daily average flux densities and $T_B^{\rm disk}$ for the IRAM NIKA2 observations of Iapetus. Uncertainties are the standard deviation of all 3–6 daily scans, weighted by the inverse variance of each individual fit. The two mixed hemisphere observations in May 2018 are very noisy due to the proximity of Iapetus to Saturn's sidelobes; these data are not used hereafter.

| Date | $r_h$ (AU) | Lat. (°N) | Long. (°E) | Region | $\nu$ (GHz) | $\lambda$ (mm) | Flux density (mJy) | $T_B^{\rm disk}$ (K) |
|---|---|---|---|---|---|---|---|---|
| 28 MAY 2018 | 10.04 | 11.3 | 155 | Mixed | 260 | 1.2 | 136 ± 7.5 | 79.6 ± 4.1 |
| | | | | | 150 | 2.0 | 46.3 ± 10.5 | 79.4 ± 17.1 |
| 29 MAY 2018 | 10.04 | 11.3 | 150 | Mixed | 260 | 1.2 | 131 ± 14.0 | 76.7 ± 7.6 |
| | | | | | 150 | 2.0 | 35.7 ± 9.5 | 62.0 ± 15.5 |
| 14 FEB 2019 | 10.07 | 9.5 | 54 | TH | 260 | 1.2 | 76.9 ± 2.3 | 64.2 ± 1.7 |
| | | | | | 150 | 2.0 | 25.8 ± 1.8 | 62.5 ± 4.0 |
| 15 FEB 2019 | 10.07 | 9.5 | 50 | TH | 260 | 1.2 | 81.4 ± 6.0 | 67.5 ± 4.5 |
| | | | | | 150 | 2.0 | 25.2 ± 2.3 | 61.0 ± 5.3 |
| 12 MAR 2019 | 10.07 | 8.9 | -61 | LH | 260 | 1.2 | 110.3 ± 2.9 | 84.4 ± 2.1 |
| | | | | | 150 | 2.0 | 41.4 ± 3.5 | 92.4 ± 7.4 |
| 20 MAR 2019 | 10.05 | 8.8 | -97 | LH | 260 | 1.2 | 97.7 ± 7.2 | 73.7 ± 5.0 |
| | | | | | 150 | 2.0 | 40.9 ± 2.5 | 89.0 ± 5.2 |
| 21 MAR 2019 | 10.05 | 8.8 | -101 | LH | 260 | 1.2 | 101.8 ± 6.8 | 76.2 ± 4.7 |
| | | | | | 150 | 2.0 | 42.0 ± 4.1 | 91.0 ± 8.5 |

To measure the flux densities of the LH and TH of Iapetus independently, observations of the satellite occurred near maximum elongation, which occurs every 40 days (for the LH then the TH), which was also beneficial in minimizing the impact of Saturn through its sidelobes. Data were acquired on the TH on two occasions (14 and 15 February 2019); on the LH on three (12, 20, and 21 March 2019), and on a mixture of leading and trailing four times (23, 27, 28, and 29 May 2018). A preliminary analysis of these data has been presented in Bonnefoy et al. (2020b). For observations sampling a mix of LH and TH, i.e. taken far away from maximum elongation, it is very difficult to correctly measure the flux density from Iapetus due to its proximity to Saturn; furthermore, these data are not useful for characterisation of the pure LH and TH; we will therefore not discuss the May 2018 data herein.

On each day, we used the NIKA2 camera to image a field of view centered on Saturn and extending at least 100" beyond the position of Iapetus. Had the observations been centered on Iapetus, the very bright

planet Saturn would have leaked through the telescope beam sidelobes into the map and generated strong artefacts. Each individual scan took 6 minutes; to increase the SNR, three or four series of six scans were conducted and averaged each day. For each scan, the Iapetus flux density and its 95% confidence interval was extracted by fitting a 2D Gaussian on a tilted plane to the image. The calibration was performed on Titan and Saturn which present the advantage of being observed simultaneously to Iapetus (unlike the other calibrators such as Uranus). The IRAM NIKA2 observations of Iapetus and their calibration on Titan and Saturn are detailed in Appendix A.

Iapetus flux density is finally converted to $T_B^{\rm disk}$ following the method described in Section 3.1. The flux densities of all 3–6 daily scans are averaged, using the inverse variance of each individual fit as weights; the uncertainties are the weighted standard deviation. The daily average disk-integrated flux densities and brightness temperatures are provided in Table 3 and shown in Fig. 2. As expected, the leading side, which is covered by the optically dark material, has significantly higher $T_B^{\rm disk}$ than the trailing side, especially at 2.0 mm.

### 3.3. *IRAM Northern Extended Millimeter Array (NOEMA) observations*

The NOrthern Extended Millimeter Array (NOEMA) is a millimeter-wavelength interferometer located at the Plateau de Bure in the French Alps. Like the 30-meter dish at Pico Veleta, this twelve-antenna array is operated by the IRAM. This instrument, unique in the Northern hemisphere, was crucial to confirm or infirm the puzzling 3.3-mm observation of the Iapetus LH and the possible scattering feature of the TH (Ries 2012).

On 10 different dates, observations of Iapetus and Titan were acquired near maximum elongation with integration times varying from one to three hours (project W20AA). Observations are centered at either 2 mm (150 GHz) or 3.3 mm (100 GHz), with in each case four separate frequency bands, with two different polarizations (vertical and horizontal) each. Similarly to the IRAM NIKA2 observations, it is possible to calibrate the Iapetus flux densities on Titan, which can be observed at the same time and thus under the

**Table 4.** Average flux densities and $T_B^{\rm disk}$ for the IRAM NOEMA observations of Iapetus. The effective frequency $\nu_{eff}$ is the average of the eight observed sub-bands (four frequencies and two polarizations), weighted by the inverse variance of the fluxes in each sub-band. Uncertainties in flux and $T_B^{\rm disk}$ are the weighted standard deviations of all eight observations.

| Date | $r_h$ (AU) | Lat. (°N) | Long. (°E) | Region | $\nu_{eff}$ (GHz) | $\lambda$ (mm) | Flux density (mJy) | $T_B^{\rm disk}$ (K) |
|---|---|---|---|---|---|---|---|---|
| 17 DEC 2020[a] | 9.93 | 6.4 | -101 | LH | 86.4 | 3.44 | 13.4 ± 2.8 | 91.5 ± 3.2 |
| 01 MAR 2021 | 9.99 | 3.9 | -70 | LH | 146 | 2.06 | 33.4 ± 4.0 | 84.2 ± 3.2 |
| 02 MAR 2021 | 9.98 | 3.8 | -73 | LH | 95.5 | 3.13 | 15.4 ± 2.4 | 87.5 ± 0.8 |
| 07 MAR 2021[b] | 9.97 | 3.7 | -96 | LH | 89.6 | 3.37 | 11.9 ± 2.1 | 77.1 ± 2.6 |
| 08 MAR 2021 | 9.97 | 3.7 | -100 | LH | 138 | 2.17 | 31.5 ± 3.3 | 86.1 ± 0.8 |
| 08 MAR 2021 | 9.97 | 3.7 | -100 | LH | 89.8 | 3.38 | 13.1 ± 2.3 | 84.9 ± 0.8 |
| 11 APR 2021 | 9.96 | 2.8 | 108 | TH | 145 | 2.07 | 27.2 ± 3.1 | 63.1 ± 0.9 |
| 12 APR 2021 | 9.97 | 2.8 | 104 | TH | 93.8 | 3.36 | 10.4 ± 1.8 | 61.8 ± 1.5 |
| 16 APR 2021[a] | 9.97 | 2.7 | 86 | TH | 95.8 | 3.20 | 12.4 ± 3.4 | 67.4 ± 7.3 |
| 18 APR 2021 | 9.98 | 2.7 | 77 | TH | 94.6 | 3.15 | 10.9 ± 1.9 | 56.5 ± 2.3 |
| 21 APR 2021[b,c] | 9.98 | 2.6 | 64 | TH | 150 | 2.10 | 25.0 ± 5.1 | 59.1 ± 5.9 |

[a] On these days, the weather was poor, leading to large uncertainties (see Appendix B).

[b] On these days, the atmospheric phases of the data were irregular (see Appendix B), probably due to a turbulent atmosphere. These values are deemed not reliable and were not used in the analysis.

[c] On this day, Titan was close to Saturn, leading to uncertain calibration and large error bars.

same atmospheric conditions. After data reduction and self-calibration using the NOEMA pipeline, flux densities were measured for both Titan and Iapetus. The emission from Titan was modeled in the UV-plane at each frequency band using the spectrum from Lellouch et al. (2019). The Iapetus flux densities were then calibrated on Titan. Because Iapetus is unresolved, the flux density should be identical in both polarizations; any differences between these simultaneous observations are caused by inherent biases and uncertainties in the detectors. $T_B^{\rm disk}$ is derived from flux density using Eq. 2. For a given frequency, all eight data points (four frequency sub-bands and two polarizations) are averaged for each Iapetus observation.

The flux densities and $T_B^{\rm disk}$ averaged for each day are provided in Table 4 and shown in Fig. 2. The observation conditions are provided in Appendix B (Table B.1). At 2 mm, the NOEMA data are perfectly consistent with the NIKA2 data on the TH, and slightly lower but still within 1-$\sigma$ uncertainties on the LH.

**Table 5.** Flux densities and and $T_B^{\rm disk}$ derived from VLA observations of Iapetus and Phoebe. The region observed is indicated for Iapetus but not for Phoebe, which is not in synchronous rotation (and therefore does not have leading and trailing sides).

| Date | $r_h$ (AU) | Lat. (°N) | Long. (°E) | Region | Band | $\nu_{\rm eff}$[a] (GHz) | $\lambda$ (mm) | Flux density (μJy) | $T_B^{\rm disk}$ (K) |
|---|---|---|---|---|---|---|---|---|---|
| Iapetus observations | | | | | | | | | |
| 21 May 2018 | 10.04 | 11 | -171 | Mixed | X | 10.07 | 29.8 | 172 ± 4.8 | 65.7 ± 1.8 |
| 28 May 2018 | 10.04 | 11 | 157 | Mixed | Ka | 35.02 | 8.6 | 2008 ± 16.9 | 62.7 ± 0.5 |
| 28 May 2018 | 10.04 | 11 | 157 | Mixed | Ka | 31.02 | 9.7 | 1597 ± 15.0 | 63.5 ± 0.6 |
| 03 Jun 2018 | 10.05 | 11 | 129 | TH | K | 24.03 | 12.5 | 830 ± 20.7 | 54.9 ± 1.3 |
| 03 Jun 2018 | 10.05 | 11 | 129 | TH | K | 20.03 | 15.0 | 645 ± 16.7 | 61.0 ± 1.5 |
| 05 Jun 2018 | 10.05 | 11 | 120 | TH | Ku | 16.52 | 18.1 | 454 ± 6.8 | 62.9 ± 0.9 |
| 05 Jun 2018 | 10.05 | 11 | 120 | TH | Ku | 13.53 | 22.2 | 304 ± 5.6 | 62.8 ± 1.1 |
| 29 Aug 2019 | 10.04 | 10 | -115 | LH | X | 10.07 | 29.8 | 178 ± 5.2 | 70.0 ± 2.0 |
| 24 Jan 2021 | 9.98 | 5 | 88 | TH | C | 6.11 | 50.0 | 30 ± 5 | 46.5 ± 7.3 |
| 28 Jan 2021 | 9.99 | 5 | 71 | TH | Ku | 16.52 | 18.1 | 241 ± 6.6 | 49.1 ± 1.3 |
| 28 Jan 2021 | 9.99 | 5 | 71 | TH | Ku | 13.53 | 22.2 | 183 ± 6.1 | 55.2 ± 1.8 |
| 31 Jan 2021 | 9.99 | 5 | 58 | TH | K | 24.03 | 12.5 | 526 ± 12 | 50.6 ± 1.1 |
| 31 Jan 2021 | 9.99 | 5 | 58 | TH | K | 20.03 | 15.0 | 386 ± 11 | 53.3 ± 1.4 |
| Phoebe observations | | | | | | | | | |
| averaged[b] | 10.05 | 19 | -15 & 27 | – | K | 22.03 | 13.7 | 22.5 ± 4.1 | 90.8 ± 16.0 |
| 01 Jun 2019 | 10.11 | 19 | -36 | – | Ka | 33.08 | 9.4 | 44.8 ± 5.8 | 76.6 ± 9.4 |
| 31 May 2019 | 10.09 | 19 | 112 | – | Q | 44.06 | 6.8 | 81.8 ± 18.5 | 78.9 ± 17.2 |

[a]Effective frequency is calculated for blackbody emission across the observed frequency range.

[b]Phoebe K-band observations were taken on two dates – 12 May and 22 Jun 2019 – and averaged to increase signal-to-noise.

The NOEMA observations of the TH also suggest that the absorption feature proposed by Ries (2012) is narrower than initially thought, if present at all. At 3.3 mm, the mean NOEMA $T_B^{disk}$ is 87.9 ± 1.2 K, which lies 3$\sigma$ below the value of 100.4 ± 4.2 K observed with the GBT by Ries (2012). We conclude that the GBT value is likely overestimated due to calibration and data reduction issues at a frequency for which the telescope was not designed to operate.

### 3.4. *Very Large Array (VLA) observations*

The National Science Foundation's Karl G. Jansky Very Large Array (VLA) is a radio interferometer of 27 25-meter parabolic antennas, located on the Plains of San Agustin, New Mexico (USA). The antennas of the interferometer are moved along three arms to yield different resolution in four configurations: D (most compact); C, B, and A (most extended), with a maximum antenna spacing of ≈ 36 km in the A configuration. Frequencies from 1-50 GHz are covered contiguously in eight receiving bands. We observed in the six bands at the highest frequencies: C-band (4-8 GHz); X-band (8-12 GHz); Ku-band (12-18 GHz); K-band (18-26 GHz); Ka-band (29-37 GHz); and Q-band. To facilitate resolution of Iapetus (maximum diameter ≈ 0.21") at the higher frequencies, all of our Iapetus observations were undertaken in the A configuration. Confusion from Saturn is mainly minimized by attempting to observe at large elongation (for the leading and trailing hemispheres), when the separation of Iapetus from Saturn is maximized and Saturn is outside the main lobe of the primary beams of the antennas. Observing in the A configuration also aids in this, because it is the shorter antenna spacings that are mostly affected by Saturn confusion (on the longer baselines the emission is resolved out). As noted, the high-frequency observations of Iapetus are spatially resolved. Herein, we focus on the disk-integrated flux densities to examine the spectra of both hemispheres; future work will include spatially resolved modeling of Iapetus to examine e.g. spatial variations in dark material thickness. In addition to Iapetus, we observed Phoebe (diameter ≈ 0.03"), which is unresolved even in A configuration. Given that Phoebe cannot be resolved and Saturn contamination is not an issue at its orbital distance, Phoebe was observed in the B configuration instead of the A configuration.

Observing the leading and trailing side of Iapetus near maximum elongation, which are visible alternately for a few days every 40 days, imposes strong timing constraints which could not always be met (mostly because observing conditions were not appropriate for the frequencies needing to be observed), so that some data were actually taken on the anti-Saturn hemisphere. Data have been acquired on the TH, anti-Saturn (labelled as "mixed"), and LH sides of Iapetus, as well as on Phoebe, both of which were detected for the first time from Earth at centimeter wavelengths. Further details on the observing conditions, calibration process, and flux density determination are provided in Appendix C.

The flux densities and $T_B^{\rm disk}$ derived for Iapetus and Phoebe are provided in Table 5 and discussed in the following sections.

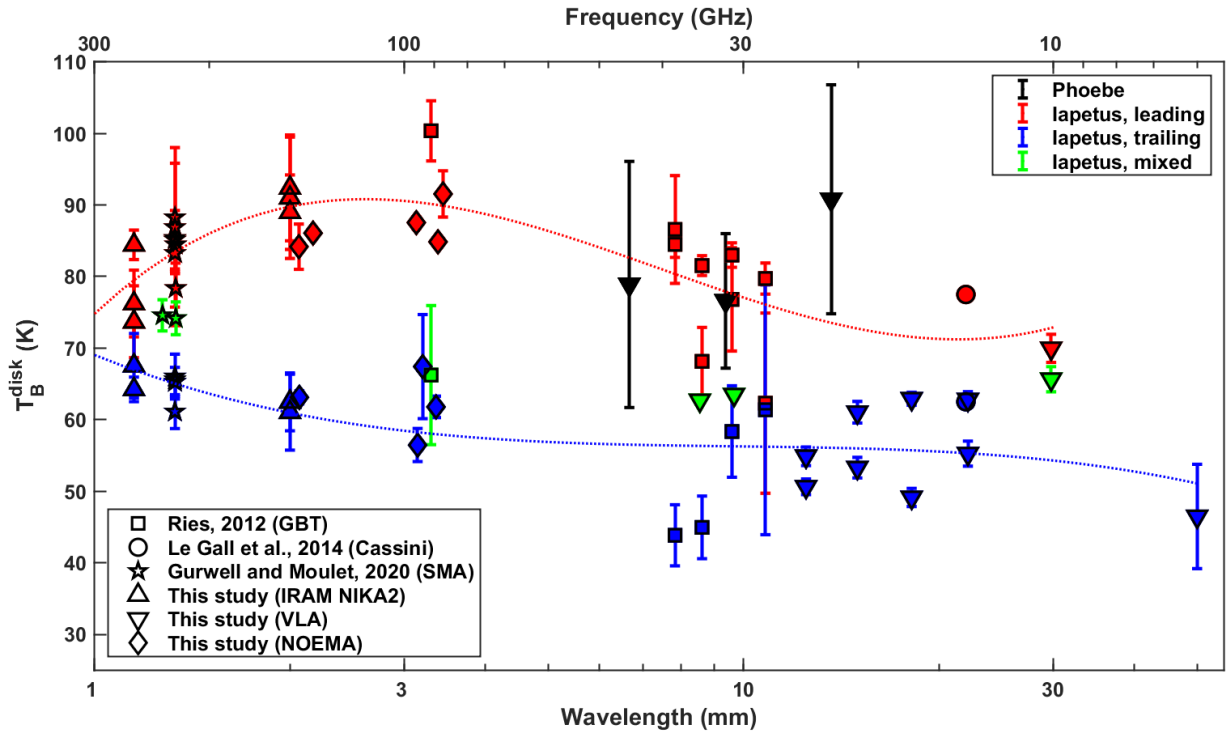


**Figure 2.** Iapetus LH and TH microwave $T_B^{\rm disk}$ spectra, including IRAM NIKA2, IRAM NOEMA, and VLA data, as well as observations from previous studies (Ries 2012; Le Gall et al. 2014, Gurwell and Moullet, 2020, personal communication). VLA observations of Phoebe are included for comparison and are discussed in Section 4.5. Dotted lines are a degree 3 polynomial fit through the data. The leading and trailing sides are defined as $-90 \pm 50°$E and $+90 \pm 50°$E, respectively, with other longitudes classified as "mixed". Note that the brighter trailing VLA 1–2 cm (K- and Ku-band) data are acquired near the edge of the trailing hemisphere and are likely affected by the dark material.

### 3.5. *The LH and TH microwave spectra of Iapetus*

The sub-observer coordinates of all reliable existing Earth-based microwave observations of Iapetus to date, as well as two Cassini radiometry observations, are displayed in Fig. 3. The updated Iapetus LH and TH spectra are shown in Fig. 2, along with the VLA observations of Phoebe. The difference in $T_B^{\rm disk}$ between the LH and TH of Iapetus is apparent at all observed millimeter to centimeter wavelengths. As expected from the leading/trailing optical albedo dichotomy and from Cassini data (Le Gall et al. 2014), the (low-albedo) LH is always radiometrically warmer than the trailing side, at least on its day side. In order to determine whether an albedo difference is sufficient to account for this dichotomy (see Section 4) or if other

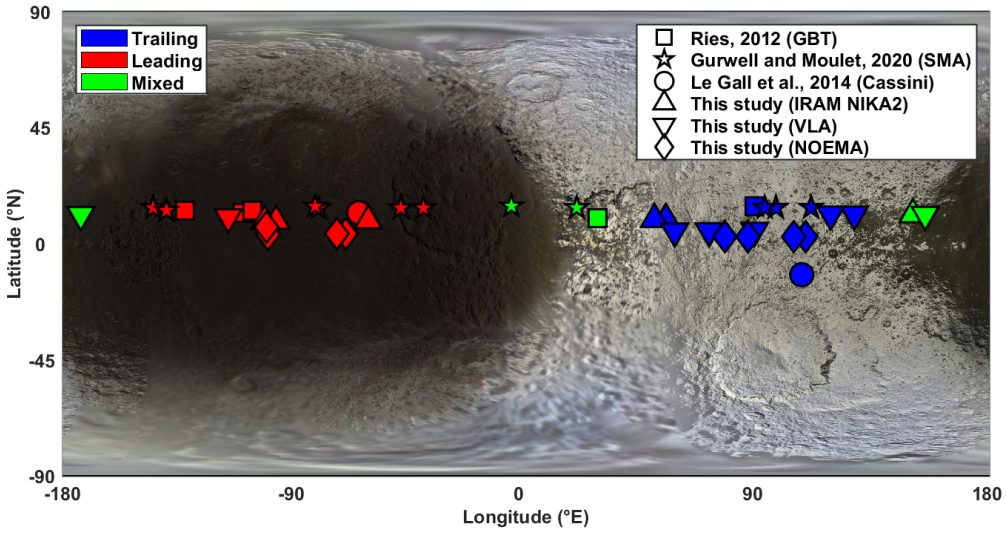


**Figure 3.** Map of Iapetus with the sub-observer point indicated for each date of observation acquired both before (Ries 2012; Hagen et al. 2014, Gurwell and Moullet 2020, personal communication) and during the present study. The sub-spacecraft points of the two Cassini radiometry observations used herein are also shown. LH, TH, and mixed locations are shown in red, blue, and green, respectively. The background image is the ISS 3-color composite of Iapetus (PIA18436).

properties such as emissivity are also responsible for Iapetus hemispheric dichotomy, a subsurface thermal model is required. Comparison to such a model is discussed in Section 4.

**Leading hemisphere** $T_B^{\rm disk}$ measured on the LH by the IRAM NIKA2 camera at 1.2 and 2.0 mm, the SMA 1.3 mm, NOEMA at 2 and 3 mm, and the GBT at 3.3 mm all indicate an increasing $T_B^{\rm disk}$ with wavelength. This is a surprising result: indeed, for daytime observations, the surface should be warmer than the subsurface and since the probed depth is roughly proportional to the wavelength, $T_B$ should decrease with $\lambda$. As noted in Section 3.3, the IRAM NOEMA 3.1–3.4 mm data are inconsistent with the GBT 3.3 mm LH observation from Ries (2012), which may require further calibration checks. Beyond 3.3 mm and up to 3 cm, $T_B^{\rm disk}$ decreases, either because the subsurface is colder and/or because the contribution from a lower emissivity layer increases.

**Trailing hemisphere** On the TH, $T_B^{\rm disk}$ appears mostly to be slightly decreasing with wavelength from 1.2 to 3.3 mm, although NIKA2, SMA, and NOEMA data are all constant within uncertainties. At longer wavelengths, the temperature may be roughly constant with wavelength but lower than at millimetric wavelengths, around 50 to 60 K, likely indicating either low physical temperatures at depth or low emissivities caused by strong scattering. In general, these results show that the TH $T_B^{\rm disk}$ is higher at millimetric rather than centimetric wavelengths, opposite to what was observed by Ries (2012) with the GBT.

**Trailing hemisphere cm-wavelength discrepancies** The VLA trailing hemisphere data actually vary in sub-observer longitude from 58 to 129° E, and can contain some low-albedo material, as shown in Fig. 4. The January 2021 K and Ku band (1.3 and 2.0 cm) $T_B^{\rm disk}$ are 7–12 K lower than those acquired in June 2018, which covered slightly more optically dark areas. It is surprising that such a small additional coverage of low-albedo material could change the centimetric $T_B^{\rm disk}$ so much, especially since the thickness of this material is expected to be small this far from the leading hemisphere. The Cassini 2.2 cm observation is also $\sim$ 10 K higher than the 2021 TH Ku band VLA. At the local time of the Cassini sub-spacecraft point (9:54 AM), the surface should be colder than at local noon (Earth-based data), so local time does not explain the discrepancy. The distance to the Sun (see Tables 2 and 5) is lower for the Cassini observations than for both the VLA 2018 and 2021 data (between which there is only a small difference), however it can only account for a $< 5$ K discrepancy (from the thermal model and depending on thermal inertia). The Cassini TH observation is slightly on the anti-Saturn side and southern hemisphere (-12°N, 107°E). Barring a very large calibration problem, the only explanation therefore appears to be regional variations within the trailing hemisphere, with the anti-Saturn side appearing more radiometrically warm at centimetric wavelengths. This oddity can be further investigated by modeling and analysing the resolved observations, rather than the disk-integrated flux densities.

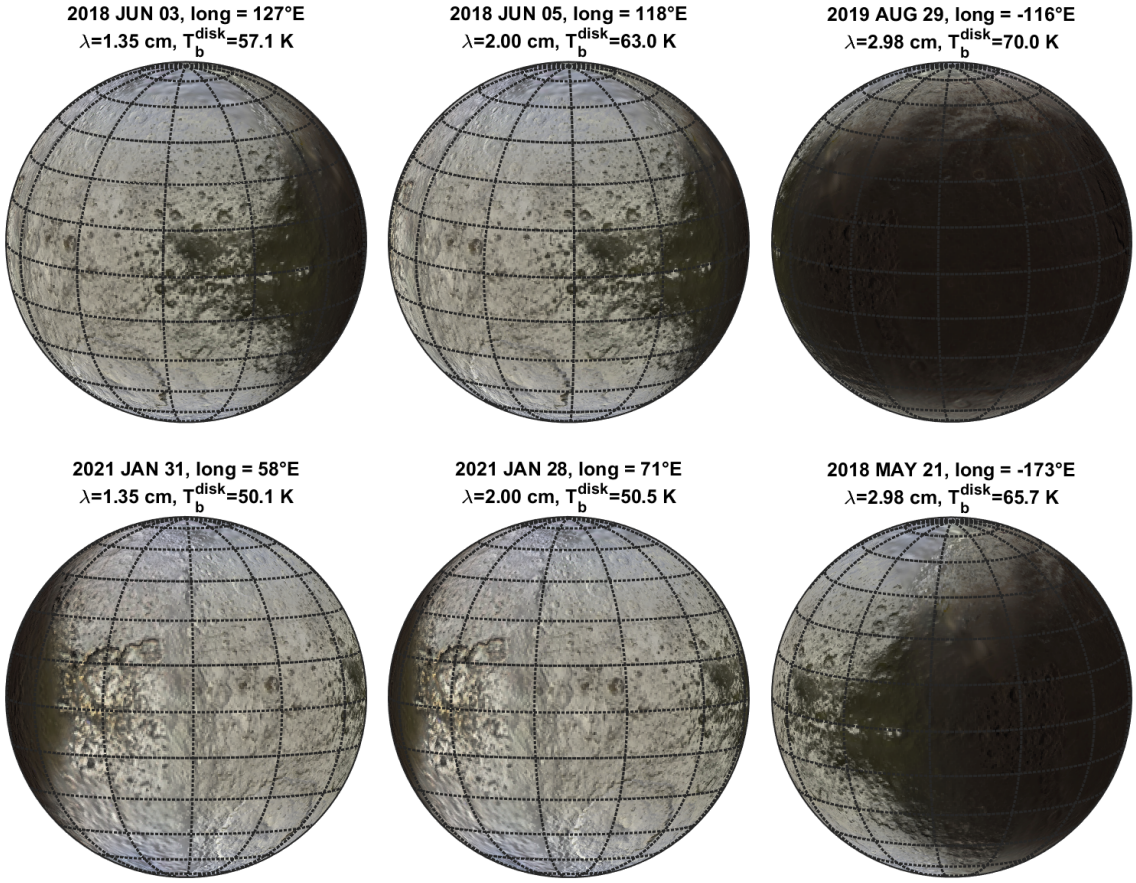


**Figure 4.** Iapetus disk for the VLA K, Ku, and X band observations, with the resulting $T_B^{\rm disk}$ indicated.

## 4. COMPARISON TO A THERMAL AND RADIATIVE TRANSFER MODEL

### 4.1. *Modeling microwave thermal emission*

The thermal and radiative transfer models applied to the Cassini 2.2 cm radiometry of Iapetus (Le Gall et al. 2014), Rhea (Bonnefoy et al. 2020a), and Saturn's other icy satellites (Le Gall et al. 2023) can also be applied to observations at other wavelengths. The model uses the bolometric Bond albedo map of Iapetus from Blackburn et al. (2011), time-varying incident local solar fluxes, and several different values of thermal inertia $I$ as inputs to solve the 1-D heat equation and derive the temperature profile with depth $z$ increasing downwards, $T(z, I)$. The temperature profile $T(z, I)$ is calculated over the whole surface with a resolution of 10°in latitude and longitude.

The effective temperature map $T_{\rm eff}(x, y)$ is computed for each point $(x, y)$ over the visible disk (centered on the sub-observer point at $x = 0, y = 0$) as follows:

$$T_{\rm eff}(x,y) = \frac{\int_0^\infty T(z, I, lat, long) e^{-\sec\theta' z/\delta_{\rm el}} dz}{\int_0^\infty e^{-\sec\theta' z/\delta_{\rm el}} dz} \quad (4)$$

with $\delta_{\rm el}$ the electrical skin depth, *lat*, *long* the coordinates at the coordinates $x, y$ on the visible disk, and $\theta'$ the angle of transmission into the subsurface, calculated from the emission angle $\theta$ as:

$$\cos\theta' = \sqrt{1 - \frac{\sin^2\theta}{\varepsilon'_r}} \quad (5)$$

with $\varepsilon'_r$ the real part of the complex permittivity, taken to be 1.15 (Bonnefoy et al. 2020a; Le Gall et al. 2023). The effective temperature map thus accounts for the fact that shallower depths are probed at high emission angles. As in Le Gall et al. (2014); Bonnefoy et al. (2020a); Le Gall et al. (2023) and as detailed in Table 6, the parameters of this model are the thermal inertia $I$ and the ratio of electrical to thermal diurnal skin depth $r = \delta_{\rm el}/\delta_{\rm th}^{\rm day}$. The effective temperature map is then integrated over the disk to obtain $T_{\rm eff}^{\rm disk}$. Lastly, the simulated brightness temperatures $T_B^{\rm disk}$ are found by using the Planck equation for $B_\nu$ and varying the microwave emissivity $e$ from 0.5 to 1:

$$B_\nu(T_{\rm B}^{\rm disk}) = e \times B_\nu(T_{\rm eff}^{\rm disk}) \quad (6)$$

The simulated $T_B^{\rm disk}$ are directly comparable to those measured by Earth-based radiotelescopes. As expressed here, the emissivity depends both on the dielectric properties of the medium (complex relative permittivity $\varepsilon_r = \varepsilon'_r + i\varepsilon''_r$) and on its scattering properties (surface roughness and subsurface scattering), which cannot be discriminated in this model. In other words, losses due to absorption and scattering cannot be separated. For instance a very low emissivity is indicative of a high dielectric constant and/or a heterogeneous medium with efficient scatterers. Volume scattering, caused by the presence of numerous heterogeneities (voids, particles, cracks…) in a low-loss medium, leads to low microwave emissivity and is likely responsible for the emissivities observed by the Cassini Radar/radiometer on Saturn's icy moons

**Table 6.** Parameters of the thermal and radiative transfer models

| Parameter | Symbol | Unit | Values | Comment and reference |
|---|---|---|---|---|
| Thermal inertia | $I$ | J m$^{-2}$ K$^{-1}$ s$^{-1/2}$ | 10, 20, 50, 100, 250, 500, 1000 | |
| Skin depth ratio | $r$ | - | 0.01, 0.05, 0.1, 0.5, 1, 5, 10, 50, 100, 500, 1000 | $r = \delta_{\rm el}/\delta_{\rm th}^{\rm day}$ |
| Subsurface microwave emissivity | $e$ | - | 0.5 to 1 (step of 0.01) | |
| Diurnal thermal skin depth | $\delta_{\rm th}^{\rm day}$ | m | 0.02 to 2 | Calculated from $I$ as $\delta_{\rm th}^{\rm day} = \frac{I}{\rho C}\sqrt{\frac{P_{\rm day}}{\pi}}$ |
| Electrical skin depth | $\delta_{el}$ | m | 0.001 to 1000 | $\delta_{el} = \lambda/(2\pi\varepsilon_r''/\sqrt{\varepsilon_r'})$ |
| Bolometric Bond albedo | $A_B$ | - | Map (0.01 - 0.41) | Blackburn et al. (2011) |
| Density of water ice | $\rho_{ice}$ | kg/m$^3$ | 918 | Klinger (1981) |
| Volumetric heat capacity of water ice | $C$ | Jkg$^{-1}$K$^{-1}$ | 829 | Klinger (1981) |
| Surface IR emissivity | $e_{IR}$ | - | 1 | Carvano et al. (2007); Howett et al. (2010) |

(Le Gall et al. 2023).

We assume that there are no variations of the parameters with depth, which is not realistic since it is known that at least thermal inertia increases with depth (Le Gall et al. 2014). This simplified model is nonetheless useful to test whether vertical variations are necessary in order to fit the data, or if they are only significant to second order. As summarized in Table 6, the free parameters are thermal inertia $I$, the ratio of electrical to thermal diurnal skin depth $r = \delta_{\rm el}/\delta_{\rm th}^{\rm day}$, and the emissivity $e$.

### 4.2. *Fit to the 1.3-mm SMA data : variations with longitude*

The SMA observations sample a large variety of sub-observer longitudes (Table 2): fitting this lightcurve informs on the relative importance of different parameters.

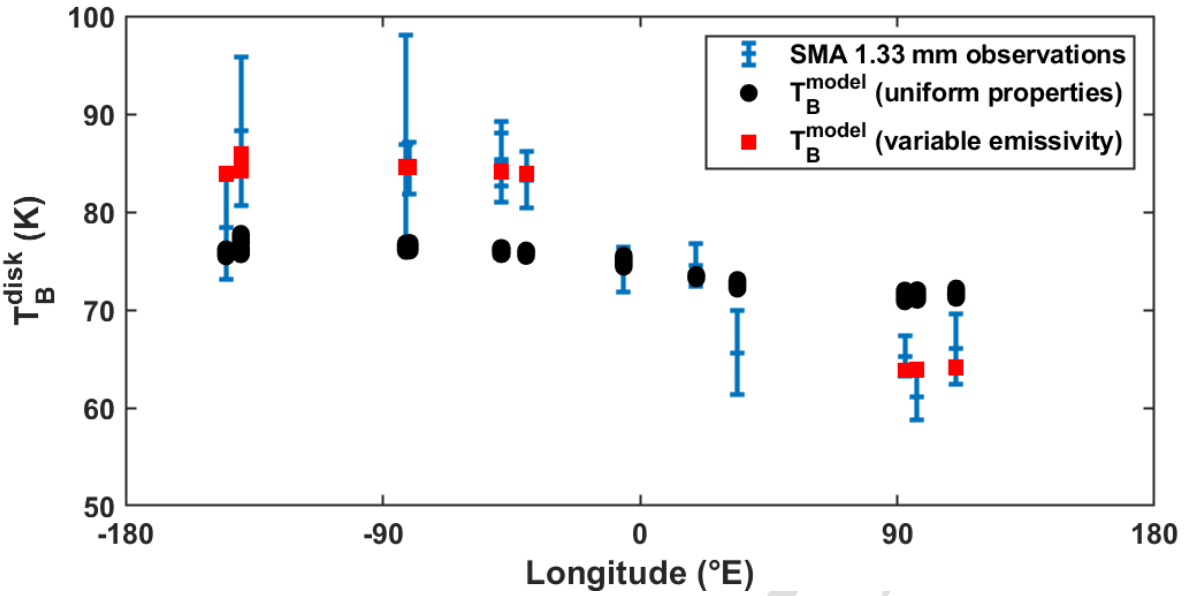


**Figure 5.** SMA 1.3 mm (225 GHz) $T_B^{\rm disk}$ measured on Iapetus, acquired and calibrated by Hagen et al. (2014) and Gurwell and Moullet (2020, personal communication). The modeled $T_B^{\rm disk}$ are shown for all tested thermal inertias $I$ and ratios $r$, while keeping the emissivity constant (black circles) or allowing it to vary between the leading and trailing hemispheres (red squares). The slight spread in $T_B^{disk}$ is due to the variable $I$ and $r$. For the specific values of emissivity at each ($I$, $r$), please refer to Fig. 7. Attempting to fit all data while keeping all parameters uniform over Iapetus is unsuccessful: the leading/trailing albedo anomaly must therefore be associated with an emissivity and/or a thermal inertia and/or a probing depth (i.e., compositional) dichotomy.

We first attempted fitting all 1.3-mm SMA observations while keeping the emissivity, thermal inertia, and skin depth ratio constant over Iapetus, thereby supposing that the leading/trailing dichotomy is primarily caused by an albedo difference well accounted for in the model. The global emissivity is calculated as the weighted average of the ratio of observed radiance $B_\nu(T_B^{\rm disk})$ to disk-averaged effective temperatures $B_\nu(T_{\rm eff}^{\rm disk}(I,r))$, with the inverse of the squared uncertainties over $T_B^{\rm disk}$ (from Table 2) used as weights. The resulting simulated $T_B^{\rm disk}$ are shown in black in Fig. 5, for all considered values of $I$ and $r$. The poor fit to the data demonstrates that an albedo dichotomy alone is insufficient (the lightcurve has an insufficient amplitude) to account for the 1.3-mm $T_B^{\rm disk}$ dichotomy, consistent with the results of Hagen et al. (2014) from an analysis of a subset of these data.

The emissivity was then derived separately for the LH ($-90 \pm 50$°E) and TH ($+90 \pm 50$°E), averaging only the data acquired in those regions. The LH and TH 1.3-mm emissivities thus obtained lead to the $T_B^{\rm disk}$ shown in red in Fig. 5. If the thermal inertia and the skin depth ratio remain uniform on all of Iapetus, then the emissivity must be at least 0.14 and up to 0.23 higher on the LH than on the TH. Similarly, if the thermal inertia and emissivity are kept uniform, then the skin depth ratio must be 10 to 100 times larger on the trailing hemisphere (and the data can only be fit for $e > 0.75$ and $I < 250$ globally). If only the thermal inertia is allowed to vary, then the LH and TH $T_B^{\rm disk}$ cannot be fitted within $< 2$ K with any of the tested ratios and emissivities, demonstrating that a thermal inertia dichotomy is insufficient. The most likely scenario is that thermal inertia, electrical skin depth, and emissivity all vary from leading to trailing sides. Indeed, all three parameters are linked to structure and composition: for example a porous material has a low thermal inertia, high skin depth ratio, and low emissivity. A higher $r$ and lower $e$ on the trailing side is consistent with a scattering and transparent/porous material, whereas the leading side is likely more uniform and absorbing.

### 4.3. *Fit to the spectra: average leading and trailing side properties*

As for the 1.3 mm SMA data, the effective temperatures have also been simulated for all other microwave observations of Iapetus described above at their epochs of measurement. The electrical skin depth, and therefore the ratio $r$, is directly proportional to the wavelength $\lambda$ (see Table 6). To simplify the considerations of skin depth for the fit, we use the skin depth ratio at 2.2 cm (Cassini Radar/radiometer wavelength) as a parameter; the ratio at other wavelengths is obtained simply as $r(\lambda) = \frac{\lambda}{2.2cm} \times r_{2.2cm}$. Assuming that all three parameters (thermal inertia $I$, skin depth ratio at 2.2 cm $r_{2.2cm}$, and emissivity $e$) are the same at all depths, we can attempt to fit the leading and trailing spectra. Because the model is computationally intensive, we ran it for a grid of parameters ($10 < I < 1000$; $0.1 < r_{2.2cm} < 1000$; $0.5 < e < 1$; see Table 6) and calculated the reduced $\chi^2$ statistic as follows:

$$\chi^2_r = \frac{1}{N-3} \sum_{i=1}^{N} \left( \frac{T_{B,i}^{\rm obs} - T_{B,i}^{\rm model}}{\sigma_i} \right)^2 \quad (7)$$

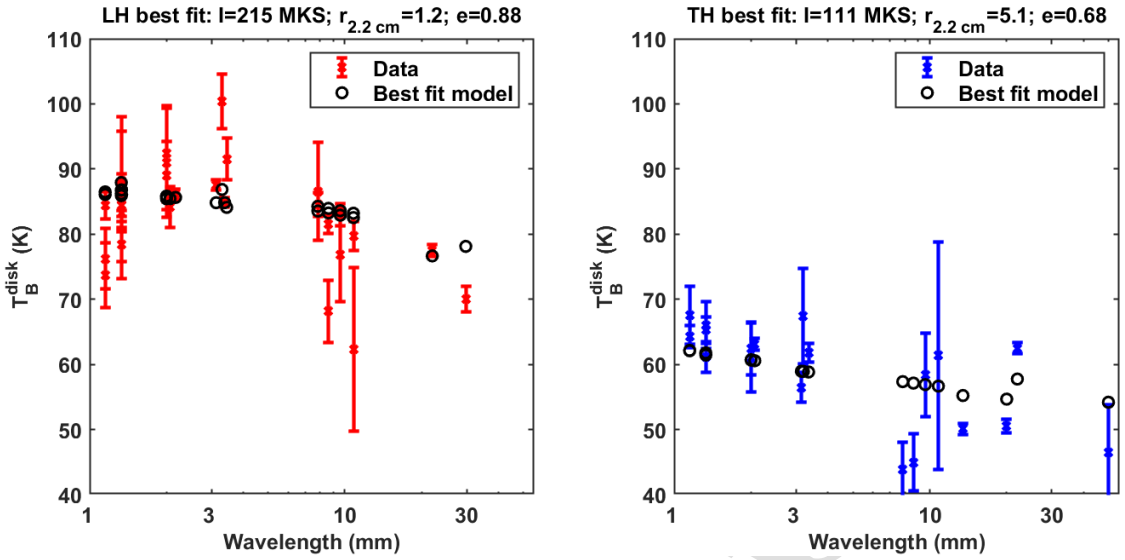


**Figure 6.** Fit of the thermal model to the (left) leading and (right) trailing hemisphere observations. For all parameters, the model is unable to fit the leading side 1–3 mm slope or the trailing side 6 mm–5 cm jumps in $T_B^{disk}$.

with $T_{B,i}^{\rm obs}$ and $T_{B,i}^{\rm model}$ the observed and modeled $T_B^{\rm disk}$ for each observation $i$, $\sigma_i$ the corresponding standard deviation, and $N$ the total number of observations (19 for the TH, 29 for the LH). The result of the fit is shown in Fig. 6; note that the VLA K and Ku-band TH observations of June 3 and 5 2018 are not included because they might be affected by the optically dark material. The $\chi^2_r$ values found are rather high (the lowest value is $\chi^2_{r,min} \approx 3.2$), due both to the inadequacy of vertically uniform thermal properties and to the occasional inconsistency of the data (e.g. at 3 mm). The best fitting spectra and values are given in Fig. 6. Given the poor quality of the fit, we do not provide uncertainties on the derived best-fit parameters, which do not represent well the surface of Iapetus: these values are merely indicative of the difference between leading and trailing hemisphere. We note that the thermal inertia and 2.2-cm skin depth ratios are consistent with the values derived from the resolved Cassini radiometry on Iapetus by Le Gall et al. (2014). The emissivity we find for the LH (0.88) is also very close to their value (0.87). However, our TH emissivity (0.68) is significantly lower than the one they found at high latitudes (0.78), either because of the poor fit to the data or due to the possible presence of dark material in the high latitude regions analyzed by Le Gall et al. (2014).

### 4.4. *Emissivity variations with wavelength*

Here, we examine the variations of thermal inertia, skin depth ratio, and emissivity with wavelength, by finding the emissivity from Eq. 6 corresponding to each ($I$,$r$) combinations. The data are averaged per band and per observatory, using the inverse of the squared uncertainties as weights. The resulting emissivity maps are shown in Fig. 7 for both the leading and trailing hemispheres. The GBT 3.3 mm LH observation is averaged with the NOEMA 3.3 mm LH data. The VLA K and Ku-band TH observations of June 3 and 5 2018 are not included because they might be affected by the optically dark material. Uncertainties on the emissivity are propagated from the uncertainties on $T_B^{disk}$. Electrical skin depths shown in the figure are calculated assuming zero porosity, and are thus strict minimum values for each ($I$,$r$) combination.

**The leading/trailing emissivity difference:** Regardless of the values of $I$ and $r$, the emissivity of the leading hemisphere must be significantly higher than on the trailing hemisphere, at all observed frequencies. This phenomenon is indicative of differences in dielectric properties (i.e., composition) and/or structure (i.e., grain size, porosity, fractures).

**The high emissivity of the LH dark material**, especially at 2 and 3.3 mm, favors materials with a low dielectric constant. Indeed, assuming a simple smooth surface governed by the Fresnel equations, the emissivity and dielectric constant are inversely related (e.g. Le Gall et al. 2011): $e > 0.95$ implies $\varepsilon'_r < 2.5$. Such dielectric constants are within the range observed on Saturn's satellites at 2.2 cm (Janssen et al. 2016; Bonnefoy et al. 2020a; Le Gall et al. 2023) and are consistent with tholins, $CO_2$ ice, or porous water ice, assuming little frequency variation (Paillou et al. 2008). The high emissivity also implies that the scattering efficiency at millimeter wavelengths must be very low, indicating either a very fine-grained and homogeneous material without dielectric discontinuities, and/or a high imaginary component of the permittivity $\varepsilon''_r$ indicative of microwave absorbing compounds. In both cases, a high dielectric medium such as a silicate regolith is inconsistent with the data. We note also that the emissivities for some combinations of ($I$,$r$) are beyond 1 and are thus nonphysical: these ($I$,$r$) combinations must be discarded. The remaining options imply either high thermal inertia (>200 MKS), which is not expected for Iapetus (Howett et al. 2010; Rivera-Valentin et al. 2011; Le Gall et al. 2014), or relatively low skin depths ratios $r < 5$. However,

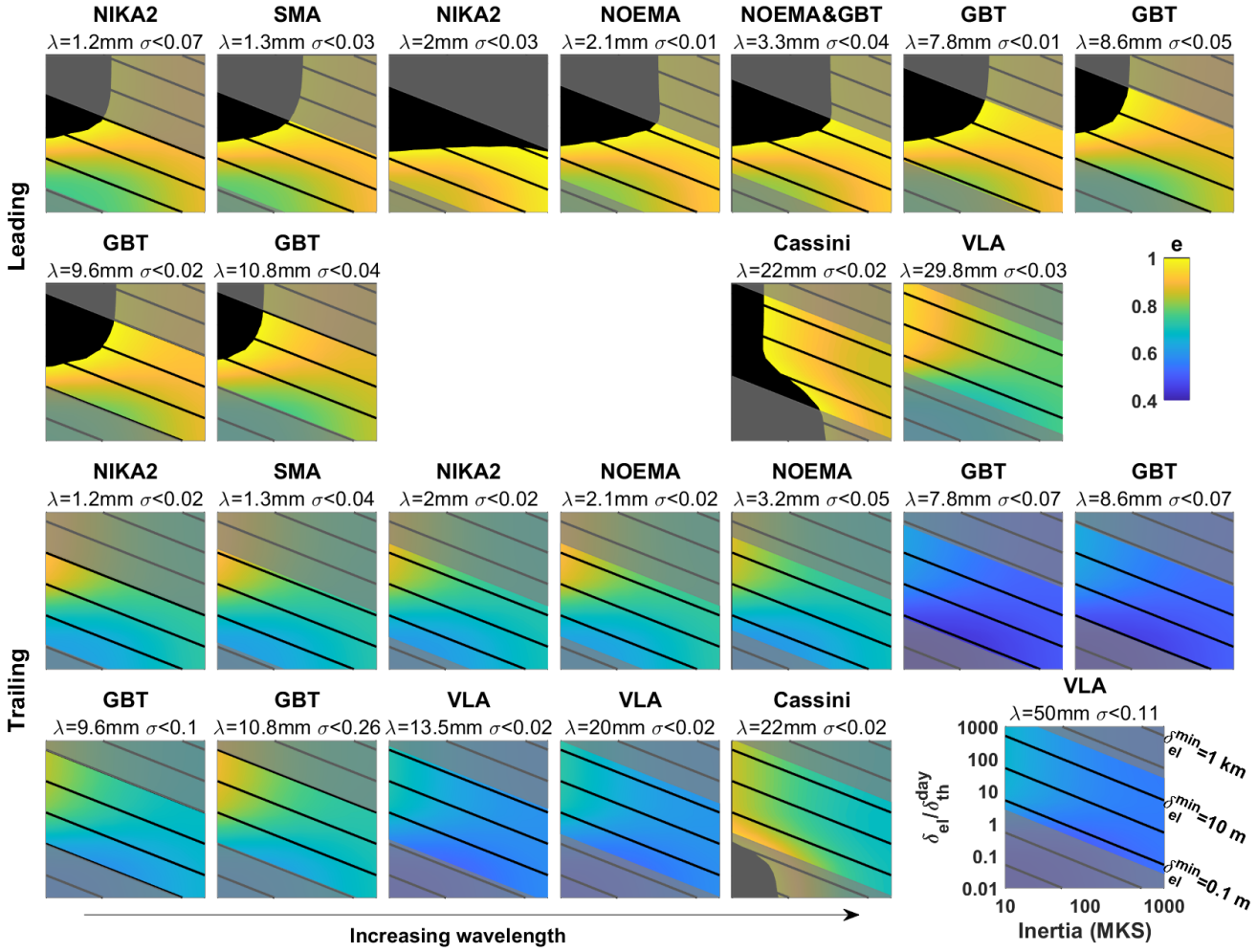


**Figure 7.** Leading and trailing hemisphere emissivities derived for each thermal inertia, skin depth ratio combination. Electrical skin depths $\delta_{el}^{min}$ are calculated assuming zero porosity, and are thus minimum values for each ($I$,$r$) combination. Black zones correspond to $e > 1$, which is non-physical. The shaded regions correspond to ($I$,$r$) combinations where $\delta_{el}^{min} < \lambda$ or $\delta_{el}^{min} > 1000\lambda$ ; they are unlikely to be valid. The maximum value of the uncertainty on the emissivity, propagated from those on $T_B^{disk}$, is indicated for each wavelength.

because the porosity is unknown and we have no lower bound on the skin depth, we cannot put constraints on the loss tangent of the material.

Meanwhile, **the low emissivities of the high-albedo TH terrain** are indicative of a scattering and low-loss medium. As for Saturn's other icy satellites, the most likely explanation is porous water ice with

many scattering structures (e.g., large grains, fractures, pores), although the shape, distribution, and origin of these scatterers remains a mystery (Bonnefoy et al. 2020a; Le Gall et al. 2023).

**The increasing 1.2 to 3.3 mm slope on the leading hemisphere** , apparent in the $T_B^{\rm disk}$ (see Fig. 2), cannot be caused by temperature variations with depth alone. Indeed, Earth-based observations are acquired on the day side, when the Sun is warming the surface. The surface (i.e., probed by shorter wavelengths) is therefore expected and modeled to be warmer than the subsurface (probed by longer wavelengths) for all Earth-based observations. Instead, the observed slope implies variations of either the emissivity or the thermal inertia and skin depth. From Fig. 7, we see that keeping the same emissivity from 1.2 to 3.3 mm would imply a decreasing thermal inertia or a decreasing electrical skin depth with increasing wavelength. This is highly unlikely given that the thermal inertia is expected to increase with depth as the medium becomes more compact (Le Gall et al. 2014) and it is difficult to imagine a medium composed of the expected materials (mostly water ice with possibly $CO_2$, tholins, iron, or silicates) where longer wavelengths would probe shallower depths. Emissivity variations with wavelength are therefore the most probable explanation.

We can think of four possible explanations for such a gradient in emissivity over the top few centimeters of the subsurface. i) The dark material particle size could be of the order of $a \approx \lambda/2\pi < 200$ µm, where $\lambda \leq 1.2$ mm is the wavelength at which Mie scattering is most active. ii) There could be a thin layer of low-emissivity material on top of the optically dark and high emissivity material. iii) Scattering could be less efficient at longer wavelengths not only because of the restricted particle sizes but also because increasing compaction with depth prevents the wave from probing much deeper at longer wavelength, thereby decreasing the number of opportunities for scattering. iv) Scattering may also be caused by empty pores themselves rather than grains. As the porosity decreases with depth or as the pores become filled with e.g. water ice, scattering would quickly become less efficient. These hypotheses are not mutually exclusive, and are all consistent with a rapidly increasing degree of compaction of the regolith with depth. An increasingly compacted subsurface would also increase the thermal inertia, consistent with the low sub-millimeter values found by CIRS ($I = 14^{+7}_{-8}$ MKS; Howett et al. (2010) and $I = 11$–$14.8$ MKS; Rivera-Valentin et al. (2011)) and the higher 2.2-cm value found by the Cassini radiometer ($I > 50$ MKS; Le Gall et al. 2014);

this increase in compaction may occur primarily within the top few centimeters. Note also that increasing the thermal inertia at larger depths would imply a further enhancement of the spectral variation of the emissivity, as pictured in Fig. 7. Future work should investigate these hypotheses further using thermal and radiative transfer models that include both vertical variations and scattering.

**The decreasing 3.3 to 30 mm leading hemisphere** $T_B^{\rm disk}$ can only be partly accounted for by decreasing temperatures at depth. Fig. 6 shows that $T_B^{\rm disk}$ is expected to decrease with increasing wavelength as we are probing more night-time temperatures. Yet, Fig. 7 shows that the emissivity must decrease significantly from millimeter wavelengths to the VLA 3 cm observation. Our interpretation is that, beyond 3.3 mm wavelengths, radiometers are beginning to probe the icy substrate underlying the high-emissivity layer, as proposed by Le Gall et al. (2014). At 7.8 mm to 22 mm, most of the material probed still consists in the same high-emissivity material, but the icy substrate is increasingly detected. At 30 mm, a sharp drop in emissivity occurs, likely indicating that a significant part of the signal now originates from the water ice layer. These results are generally consistent with a leading hemisphere high-emissivity material thickness of the order of decimeters, with the possible existence of a mixed transition zone.

**The trailing hemisphere** $T_B^{\rm disk}$ **and emissivities** present some inconsistencies from one observation to another. More specifically, the GBT 7.8 and 8.6 mm measurements, the Cassini TH observation, and the June 2018 VLA data are $>$ 10 K brighter than the other GBT and VLA trailing hemisphere data (Figs. 6, 4, and 7). Regardless, the TH $T_B^{\rm disk}$ generally are decreasing with increasing wavelength, a behavior which, similarly to the LH, can be caused by the colder subsurface temperatures for daytime observations. Vertical variations of the parameters remain likely, especially to explain the lower GBT and VLA data.

**The low trailing hemisphere emissivities** indicate important scattering in the subsurface. Scattering by fairly large particles or fractures, which would become more significant at longer wavelengths, might also be causing the decreasing TH $T_B$. Based on the GBT data, Ries (2012) hypothesized that 1–2-mm-size particles would decrease the emissivity at millimeter wavelengths but become insignificant at centimeter wavelengths. The new 1–3.3-mm $T_B$ of 60–70 K are higher than expected if there was significant scattering only by mm-sized grains, and the low VLA centimeter TH $T_B$ (around 50 K) indicate scattering by larger structures. A grain size gradient, increasing with depth as is often observed in snow on Earth (e.g., Brucker

**Table 7.** Phoebe disk-integrated emissivities, obtained by averaging all emissivities and associated uncertainties from Fig. 8.

| | 12 May & 2019 | 31 May 2019 | 01 Jun 2019 |
|---|---|---|---|
| Wavelength | 13.6 mm (K-band) | 9.4 mm (Q-band) | 6.8 mm (Ka-band) |
| $T_B^{\rm disk}$ (K) | 90.8 ± 16.0 | 76.6 ± 9.4 | 78.9 ± 17.2 |
| Emissivity | 0.96 ± 0.28 | 0.86 ± 0.11 | 0.91 ± 0.20 |

et al. 2010), or the presence of fractures in the icy bedrock under the porous regolith, would for example be consistent with the data.

### 4.5. *Comparison with Phoebe*

The same method used above for Iapetus is applied to the VLA observations of Phoebe. Using the same thermal model described in Section 4.1, we predict the effective temperature for different values of $I$ and $r$, from which we derive the emissivity maps shown in Fig. 8. Because Phoebe rotates quite fast (rotational period of 9.36 hours) and has an inclination of 176°to the ecliptic (i.e., close to 180°), the effect of the diurnal and seasonal waves is much less apparent than for Iapetus, and the maps are more uniform. The averaged emissivities and associated uncertainties for each observation are displayed in Table 7. Phoebe's emissivity is constant within 1-$\sigma$ uncertainties, at $e = 0.8 - 1$, similar to those found by Ostro et al. (2006); Le Gall et al. (2023) from Cassini 2.2-cm radiometry. These values are also close to those found on the LH of Iapetus at the same wavelengths (Fig. 7), but are higher than the TH emissivities for all values of the thermal inertia and skin depth (Fig. 7). This result is consistent with the hypothesis that the optically dark material covering the LH of Iapetus originates from the Phoebe ring, which likely originates from Phoebe itself (Tosi et al. 2010; Spencer & Denk 2010; Hamilton et al. 2015). These high emissivities imply that the contribution of subsurface scattering at cm wavelengths is low, indicating a fine-grained medium with few dielectric discontinuities.

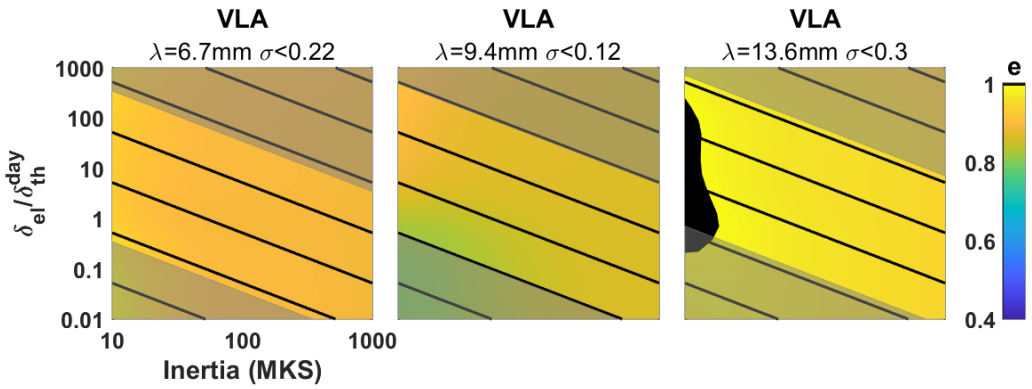


**Figure 8.** Phoebe emissivities for each thermal inertia, skin depth ratio combination. Electrical skin depths are calculated assuming zero porosity, and are thus minimum values for each ($I$,$r$) combination. The shaded gray regions correspond to minimum probed depths either shorter than the wavelength or larger than 1000 times the wavelength; they are unlikely to be valid. The maximum value of the uncertainty on the emissivity, propagated from those on $T_B^{disk}$, are indicated for each wavelength. Note that on 12 May 2019 (rightmost panel), all emissivities are > 1, indicating that the $T_B^{\rm disk}$ was most likely over-estimated.

## 5. CONCLUSION

We have acquired, calibrated, and analyzed new microwave observations of the Iapetus leading and trailing hemispheres (LH and TH) using the VLA, IRAM NOEMA, and IRAM 30-meter dish. Combining these and pre-existing $T_B^{\rm disk}$, we assemble the microwave spectrum for each hemisphere. Using a thermal and radiative transfer model with an albedo map and vertically uniform properties, we simulate the physical temperatures with depth, which, while accounting for observation geometry and frequency, are integrated over depth and over the apparent disk to yield simulated disk-integrated brightness temperatures. These are compared to the observations to obtain constraints on the sub-surface composition and structure. Our main conclusions are listed below.

- The TH is colder than the LH at all observed frequencies. This difference cannot be accounted for from albedo variations alone, but indicates that the TH has lower emissivity and is likely more transparent to microwaves than the LH.
- The results on the optically bright trailing hemisphere are consistent with an icy and very scattering regolith, similar to the other icy moons of Saturn.

- Although the very high 3.3-mm value found by Ries (2012) is not confirmed by the IRAM NOEMA data, we report increasing $T_B^{\rm disk}$ on the leading side from 1.2 mm to 3.3 mm, an unexpected slope for daytime observations. These data cannot be fit using a vertically uniform thermal properties, and point to important structural and/or compositional changes in the top few cm of the surface.

- On the leading side, $T_B^{\rm disk}$ decreases at wavelengths longer than 3.3 mm, consistent with colder nighttime temperatures and/or increased probing depths into a less emissive icy substrate.

- There is a 7 to 12.5 K discrepancy between centimeter-wavelength observations (VLA and Cassini) of the trailing side at different dates, which is significant since uncertainties in the K and Ku bands are < 2 K for both instruments (Tables 2 and 5). The higher values may be caused by the presence of slightly more optically-dark material within the observed disk at some dates, especially on the anti-Saturn side (Fig. 4). This sensitivity to even small quantities of dark material would indicate that its microwave properties (complex permittivity) are very different from those of the bright icy material.

- We observed Saturn's retrograde moon Phoebe for the first time at microwave frequencies, revealing emissivities similar to the leading hemisphere of Iapetus and inconsistent with its trailing hemisphere.

To further reveal the vertical variations in structure and composition on both sides of Iapetus, future work should focus on multi-layer thermal and radiative transfer modeling. It would be particularly useful to better constrain the thickness (and its likely regional variations; Le Gall et al. 2014) of the leading hemisphere low-albedo and high-emissivity layer. Indeed, a comparison with dust deposition models (Tamayo et al. 2011) would provide the time for which exogenic dust has been depositing on the leading side of Iapetus. Meanwhile, on the trailing side, the identity, shape, distribution, and origin of the scatterers remains mysterious, similarly to the other icy moons of the solar system (e.g. Le Gall et al. 2023). To help answer these questions, the unique multi-frequency dataset assembled here can for example be analyzed with the Snow Microwave Radiative Transfer Model (SMRT), a complex radiative transfer model designed to simulate multi-frequency active and passive microwave observations of snow on Earth (Picard et al. 2018). Finally, we only used disk-integrated values for the VLA observations of Iapetus; however, these observations were resolved, and will allow further investigation into the emissivity and thermal properties of

different regions at several local times. Similarly, resolved millimetric ALMA observations would be very valuable to compare with those acquired by the VLA and to detect regional anomalies for instance related to impact craters, as found on moons of Saturn and Jupiter (Bonnefoy et al. 2020a; de Kleer et al. 2021).

## 6. ACKNOWLEDGEMENTS

This work is the result of an international effort to observe the microwave spectra of Iapetus in the microwaves. The authors warmly thank the NRAO VLA and the IRAM NIKA2 and NOEMA staff for making these new observations possible throughout the proposal review, observation campaign, data reduction, and calibration processes. The authors acknowledge financial support from the Île-de-France region DIM-ACAV+ (Domain d'intérêt Majeur en Astrophysique et Conditions d'Apparition de la Vie) project.

This work makes use of GBT, SMA, VLA, NOEMA, and IRAM 30m telescope observations. The Green Bank Observatory is a facility of the National Science Foundation operated under cooperative agreement by Associated Universities, Inc. The Submillimeter Array (SMA) is a joint project between the Smithsonian Astrophysical Observatory and the Academia Sinica Institute of Astronomy and Astrophysics and is funded by the Smithsonian Institution and the Academia Sinica. We recognize that Mauna Kea, where the SMA is located, is a culturally important site for the indigenous Hawaiian people; we are privileged to study the cosmos from its summit. VLA observations were carried out under project codes 18A-090, 19A-093, and 20B-290. The VLA belongs to the National Radio Astronomy Observatory (NRAO), which is a facility of the National Science Foundation operated under cooperative agreement by Associated Universities, Inc. Observations were carried out under project numbers 111-18 and 087-17 with the IRAM 30m telescope, and under project number W20AA with the IRAM NOEMA Interferometer. IRAM is supported by INSU/CNRS (France), MPG (Germany) and IGN (Spain). We would like to thank the IRAM staff for their support during the campaigns.

## REFERENCES

Acton, C., Bachman, N., Semenov, B., & Wright, E. 2018, Planetary and Space Science, 150, 9, doi: 10.1016/j.pss.2017.02.013

Adam, R., Adane, A., Ade, P. A. R., et al. 2018, A&A, 609, A115, doi: 10.1051/0004-6361/201731503

Black, G. J., Campbell, D. B., Carter, L. M., & Ostro, S. J. 2004, Science, 304, 553, doi: 10.1126/science.1096470

Blackburn, D. G., Buratti, B. J., & Ulrich, R. 2011, Icarus, 212, 329, doi: 10.1016/j.icarus.2010.12.022

Bonnefoy, L. E., Le Gall, A., Lellouch, E., et al. 2020a, Icarus, 352, 113947, doi: https://doi.org/10.1016/j.icarus.2020.113947

Bonnefoy, L. E., Lestrade, Jean-François, Lellouch, Emmanuel, et al. 2020b, EPJ Web Conf., 228, 00006, doi: 10.1051/epjconf/202022800006

Brucker, L., Picard, G., & Fily, M. 2010, Journal of Glaciology, 56, 514, doi: 10.3189/002214310792447806

Buratti, B. J., Cruikshank, D. P., Brown, R. H., et al. 2005, The Astrophysical Journal, 622, L149, doi: 10.1086/429800

Burns, J. A., Hamilton, D. P., Mignard, F., & Soter, S. 1996, International Astronomical Union Colloquium, 150, 179, doi: 10.1017/S025292110050150X

Butler, B., & Desai, K. 1999, Phase Fluctuations at The VLA Derived From One Year of Site Testing Interferometer Data, Vla test memo. no. 222, National Radio Astronomy Observatory

Butler, B. J., & Bastian, T. S. 1999, in ASP Conference Series, Vol. 180, Synthesis Imaging in Radio Astronomy II, ed. G. B. Taylor, C. L. Carilli, & R. A. Perley, 625–656

Calvo, M., Benoît, A., Catalano, A., et al. 2016, Journal of Low Temperature Physics, 184, 816, doi: 10.1007/s10909-016-1582-0

Carilli, C. L., & Holdaway, M. A. 1999, Radio Science, 34, 817, doi: 10.1029/1999RS900048

Carvano, J., Migliorini, A., Barucci, A., & Segura, M. 2007, Icarus, 187, 574, doi: 10.1016/j.icarus.2006.09.008

Castillo-Rogez, J. C., Hemingway, D., Rhoden, A., Tobie, G., & McKinnon, W. B. 2018, Origin and Evolution of Saturn's Mid-Sized Moons, ed. P. M. Schenk, R. N. Clark, C. J. A. Howett, A. J. Verbiscer, & J. H. Waite, 285, doi: 10.2458/azu_uapress_9780816537075-ch014

Catalano, A., Calvo, M., Ponthieu, N., et al. 2014, A&A, 569, A9, doi: 10.1051/0004-6361/201423557

Cavalié, T., Hue, V., Hartogh, P., et al. 2019, A&A, 630, A87, doi: 10.1051/0004-6361/201935954

Clark, R. N., Cruikshank, D. P., Jaumann, R., et al. 2012, Icarus, 218, 831, doi: 10.1016/j.icarus.2012.01.008

Cruikshank, D. P., Ore, C. M. D., Clark, R. N., & Pendleton, Y. J. 2014, Icarus, 233, 306, doi: 10.1016/j.icarus.2014.02.011

de Kleer, K., Butler, B., de Pater, I., et al. 2021, The Planetary Science Journal, 2, 5, doi: 10.3847/PSJ/abcbf4

Elachi, C., Allison, M. D., Borgarelli, L., et al. 2004, Space Science Reviews, 115, 71, doi: 10.1007/s11214-004-1438-9

Fink, U., Larson, H. P., Gautier, T. N., I., & Treffers, R. R. 1976, Astrophys. J, 207, L63, doi: 10.1086/182180

Hagen, N. R., Moullet, A., & Gurwell, M. A. 2014, in American Astronomical Society Meeting Abstracts, Vol. 223, American Astronomical Society Meeting Abstracts #223, 247.17

Hamilton, D. P., Skrutskie, M. F., Verbiscer, A. J., & Masci, F. J. 2015, Nature, 522, 185–187, doi: 10.1038/nature14476

Hendrix, A. R., Filacchione, G., Paranicas, C., Schenk, P., & Scipioni, F. 2018, Icarus, 300, 103, doi: 10.1016/j.icarus.2017.08.037

Hendrix, A. R., & Hansen, C. J. 2008, Icarus, 193, 344, doi: 10.1016/j.icarus.2007.07.025

Howett, C. J. A., Spencer, J. R., Pearl, J., & Segura, M. 2010, Icarus, 206, 573, doi: 10.1016/j.icarus.2009.07.016

Janssen, M., Le Gall, A., Lopes, R., et al. 2016, Icarus, 270, 443, doi: 10.1016/j.icarus.2015.09.027

Kent, B. R., Masters, J. S., Chandler, C. J., et al. 2019, in ASP Conference Series, Vol. 527, Astronomical Data Analysis Software and Systems XXIX, ed. R. Pizzo, E. R. Deul, J. D. Mol, J. de Plaa, & H. Verkouter, 571–574

Kimura, J., Kawamura, T., Morito, H., et al. 2011, Icarus, 214, 596, doi: 10.1016/j.icarus.2011.06.015

Klinger, J. 1981, Icarus, 47, 320, doi: 10.1016/0019-1035(81)90179-2

Kramer, C., Peñalver, J., & Greve, A. 2013, Tech. Rep. 2013-1

Le Gall, A., Leyrat, C., Janssen, M. A., et al. 2014, Icarus, 241, 221, doi: 10.1016/j.icarus.2014.06.011

Le Gall, A., Janssen, M., Wye, L., et al. 2011, Icarus, 213, 608, doi: 10.1016/j.icarus.2011.03.026

Le Gall, A. A., Bonnefoy, L. E., Sultana, R., et al. 2023, Icarus, 394, 115446, doi: 10.1016/j.icarus.2023.115446

Lellouch, E., Gurwell, M. A., Moreno, R., et al. 2019, Nat Astron, 3, 614, doi: 10.1038/s41550-019-0749-4

Monfardini, A., Adam, R., Adane, A., et al. 2014, J Low Temp Phys, 176, 787, doi: doi.org/10.1007/s10909-013-0985-4

Ostro, S. J., West, R. D., Janssen, M. A., et al. 2006, Icarus, 183, 479, doi: 10.1016/j.icarus.2006.02.019

Paillou, P., Lunine, J., Ruffié, G., et al. 2008, Geophysical Research Letters, 35, doi: 10.1029/2008GL035216

Perotto, L., Ponthieu, N., Macías-Pérez, J. F., et al. 2020, A&A, 637, A71, doi: 10.1051/0004-6361/201936220

Picard, G., Sandells, M., & Löwe, H. 2018, Geoscientific Model Development, 11, 2763, doi: 10.5194/gmd-11-2763-2018

Pinilla-Alonso, N., Roush, T. L., Marzo, G. A., Cruikshank, D. P., & Dalle Ore, C. M. 2011, Icarus, 215, 75, doi: 10.1016/j.icarus.2011.07.004

Ries, P. A. 2012, PhD thesis, University of Virginia, USA, doi: 10.18130/V3TV9S

Rivera-Valentin, E. G., Blackburn, D. G., & Ulrich, R. 2011, Icarus, 216, 347, doi: 10.1016/j.icarus.2011.09.006

Ruppin, F., Mayet, F., Pratt, G., et al. 2018, A&A, 615, A112, doi: 10.1051/0004-6361/201732558

Spencer, J. R., & Denk, T. 2010, Science, 327, 432, doi: 10.1126/science.1177132

Tamayo, D., Burns, J. A., Hamilton, D. P., & Hedman, M. M. 2011, Icarus, 215, 260, doi: 10.1016/j.icarus.2011.06.027

Thomas, P. C., Tiscareno, M. S., & Helfenstein, P. 2018, The Inner Small Satellites of Saturn, and Hyperion, ed. P. M. Schenk, R. N. Clark, C. J. A. Howett, A. J. Verbiscer, & J. H. Waite, 387, doi: 10.2458/azu_uapress_9780816537075-ch019

Tosi, F., Turrini, D., Coradini, A., & Filacchione, G. a. 2010, Monthly Notices of the Royal Astronomical Society, 403, 1113, doi: 10.1111/j.1365-2966.2010.16044.x

Wiesmann, A., Mätzler, C., & Weise, T. 1998, Radio Science, 33, 273, doi: 10.1029/97RS02746

Highlights

- The microwave spectra of the Iapetus leading and trailing sides have been assembled.
- Radiotelescope observations of Iapetus with VLA, NIKA2/30m, and NOEMA are described.
- The trailing side shows low emissivity, similar to Saturn's other icy moons.
- The leading side spectral slopes indicate vertical composition/structure variations.
- VLA observations of Phoebe show emissivities similar to that of Iapetus leading side.

**Declaration of interests**

☒ The authors declare that they have no known competing financial interests or personal relationships that could have appeared to influence the work reported in this paper.

☐The authors declare the following financial interests/personal relationships which may be considered as potential competing interests: